Synchrotron X-ray based particle image velocimetry to measure multiphase streamflow and densitometry

Mingming Ge [a,d], Chuanyu Sun [b,*], Xinlei Zhang [a,c], Olivier Coutier-Delgosha [d], Guangjian Zhang [a,d]

[a] *Research Center of Fluid Machinery Engineering and Technology, Jiangsu University, Zhenjiang 212013, China*
[b] *ChemTech, Department of Industrial Engineering, University of Padova, I-35131 Padova (PD), Italy*
[c] *The State Key Laboratory of Nonlinear Mechanics, Institute of Mechanics, Chinese Academy of Sciences, Beijing, China*
[d] *Kevin T. Crofton Department of Aerospace and Ocean Engineering, Virginia Tech, Blacksburg, VA 24060, USA*

ARTICLE INFO

ABSTRACT

Synchrotron-based radiation techniques are increasingly used in the field of flow condition measurements. As a complicated multiphase flow, cavitation has been investigated in a wide variety of industrial fields, to prevent damages on spillways at large dams or intensify the bacteria eradication rate during water treatments. To control the detrimental effects of cavitating flows, the dynamics of and mechanisms affecting cavitation development shall be visualized and identified in real-time. Due to the large reflection and scattering effects of multiphase flow, standard visible-light imaging technologies cannot penetrate vapor bubbles and provide extremely limited information. In this study, the synchrotron source emitted high-flux X-ray pulses are used to capture flow motion and visualize internal structures with sufficiently high spatial and temporal resolutions. The image processing procedures on raw x-ray images are developed using 2D Fourier transform (FT) and wavelet transform (WT) to implement the contrast enhancement and de-noising. Through the edge detection algorithm, tracking either seeded particles or phase interfaces inside the opaque multiphase flow can be achieved to perform the particle image velocimetry. With decomposing particle-only and particle-eliminated subplots from the X-ray phase-contrast image, the time-resolved velocity and void fraction fields are obtained simultaneously, paving a way for further flow condition analysis such as densitometry.

1. Introduction

Multiphase flow appears and has been widely investigated in nuclear, chemical, and petrochemical industries (Salgado et al., 2022). As a multiphase flow, cavitation is a phenomenon in which rapid changes of pressure in a liquid lead to the formation of small vapor-filled cavities or bubbles. The physical process of cavitation is different from boiling where the evaporation occurs when the local temperature of the liquid reaches saturation temperature. While cavitating vapor appears even at room temperature when the local pressure falls sufficiently far below the saturated vapor pressure. The evolution of bubbles creates extreme conditions at localized areas with high temperature 'hotspots' up to 5000 K, high pressures up to 1000 bar, as well as significant oxidation and erosion effects (Flannigan and Suslick, 2005). In engineering fields, the hydrodynamic cavitation often generates undesirable effects such as erosion damage, system vibration, and performance degradation of hydronic machinery (Wei et al., 2017).

To understand the internal structures of cavities and control these detrimental effects, measurement techniques to quantitatively characterize the inner phenomena inside multiphase flows have been created. As listed by Salgado et al. (2021b), Computed Tomography (CT), Gamma-ray, X-ray, Magnetic Resonance Imaging, Optical probes, Electrical Capacitance Tomography, and Radioactive Particle Tracking are just a few of the modalities available, each with its own set of benefits and drawbacks. The conventional sensors like electrical impedance probe (Ruiz-Vargas et al., 2018) and endoscope (Coutier-Delgosha et al., 2006) are widely used as intrusive and pointwise measurements of the flow fields. To enable a whole-field acquisition with little perturbation of the flow, non-intrusive optical measurement techniques have been developed to investigate this complex phenomenon (Salehi et al., 2020; Zhang et al., 2021).

Due to the opacity of cloud cavitation, high-speed photography is a useful but imperfect approach to view the global behavior of cavitation. The visible light will be diffracted from the interphases of

---

multiphase flow, thus measuring the dynamics and interior structures is challenging (Wu et al., 2017). Conversely, nuclear devices employing radiation such as X-rays (Coutier-Delgosha et al., 2007; Ganesh et al., 2016) and gamma-rays (Sætre et al., 2014) can penetrate most optically opaque matter or flows, and have innovatively emerged over the last two decades (Cotte et al., 2018). For instance, in the multiphase flow containing gas, water, and oil, it is necessary to determine the percentage of the volume of fluids, i.e., fluid volume fraction (Salgado et al., 2021a). Because of the absorption difference between gas and liquid, the photon attenuation can be used to quantify the void fraction using a calibrated density table, and further execute the densitometry with the aid of neural networks (Sattari et al., 2020).

Recent reviews on X-ray flow visualization have been made by Aliseda and Heindel (2021) who highlight the success of X-ray imaging in characterizing the most commonly studied multiphase flows (e.g., sprays, fluidized beds, bubble columns) with sufficient spatial resolution to understand the microscale dynamics. Aliseda and Heindel (2021) state that X-rays are preferred because of their better spatial resolution, as well as that X-ray sources only emit X-rays when they are powered, making them safer than γ-rays. Compared with gamma radiation, tube-source X-rays own advantages of low potential cost, higher security, and availability in medical, nuclear, and flow measurement applications with fluorescence technique (Fifield et al., 2021; Zambianchi et al., 2022).

For cavitating flow containing water and vapor, the phase-contrast X-ray imaging technique has to be utilized to investigate this multiphase flow in various types of flow channels (Coutier-Delgosha et al., 2009; Khlifa et al., 2017). To perform particle image velocimetry (PIV) through tracking vapor phase structures and seeded particles in the fluid, the advanced photon source (APS) as a third-generation synchrotron radiation source at Argonne National Lab can be applied. Different from applying tube source X-ray, the synchrotron radiation can provide the high-energy and ultra-fast coherent X-ray beam with weak interaction with the matter.

In this work, The image processing and PIV algorithms based on synchrotron X-ray images are proposed for investigating the cavitating flows. With experimental validations, the X-ray PIV approach developed allows for the simultaneous acquisition of (1) the time-resolved velocity fields of liquid flow and (2) the instantaneous and high-resolution void fraction fields of vapor.

2. Experimental setup and methods

2.1. Fast X-ray imaging technique and cavitating flow generator

The experiment was carried out utilizing the third-generation synchrotron radiations in Argonne National Laboratory (APS, Chicago, USA), in which the spatially coherent and high-energy X-ray beamlines are accessible. The APS synchrotron source is a large-scale research facility composed of a storage ring, a booster, and a linear accelerator as illustrated in Fig. 1a and Fig. 1b. An electron beam is created, accelerated, and stored by these three constituents. The electrons will release so-called synchrotron radiation when they interact with a magnetic field and have sufficient speed. Because the emission is predominantly in the X-ray band, these sources are sometimes referred to as (super-bright) X-ray sources (Cotte et al., 2018).

As shown in Fig. 1c and Fig. 1d, the X-ray source on the left side is aligned with two shutters, the scintillator, and the test section. This scintillator works as an X-ray detector which converts the X-ray beams into visible lights. A high-speed CCD camera (Photron SA-Z) is used to subsequently capture the converted lights, at different acquisition rates ranging from 6035 fps to 67,888 fps. Here, the spatial resolution of the image is set as 512 pixels × 496 pixels (1 mm× 1 mm) with the pixel size of 2 μm/pixel. To record the desired image pairs for PIV measurement, the time interval between two consecutive images shall be reduced using the frame transfer method of the camera. Thus, a

mechanical rotating chopper is used as the fast shutter to limit the time interval as small as 3.68 μs. With this time interval and a 15 m/s flow speed, the moving distance of a particle is 55 μm or 28 pixels on the image. The other slow shutter, which has a 24 ms opening period and operates at a frequency of 1 Hz, is designed to protect the beam detector and the test section by limiting the heat loads.

As shown in Fig. 2a, the test section is a Venturi-type Cavitation Generation Device (CGD) with side windows open allowing the X-ray beam to penetrate through. The hydraulic loop with this CGD section provides high-speed flow (over 15 m/s) from the left entrance as shown by the arrow. The CGD channel is characterized with a convergent angle of 18° at the inlet and a divergent angle of 8° at the outlet. The flow is accelerated in the convergent section and its pressure is decreased following the 2D Bernoulli's principle: $p + \frac{1}{2}\rho v^2 = const$. At the Venturi's throat where the pressure is decreased below the vapor pressure p_v, the cavitation bubbles are generated (Fig. 2b). In the current two-phase flow, glass particles which are hollow and silver-coated with nominal mean diameters of 10 and 17 μm, are added into the liquid following the motion of the flow together with cavitation bubbles.

The A-A cross-section profile of the Venturi channel is presented in Fig. 2c. The Venturi channel width is 5 mm and the height at the throat (h_{th}) is 10 mm (Ge et al., 2021, 2022b). The heights (h_{ve}) at the channel outlet and inlet are the same 21 mm. Two pressure sensors (Keller M5HB,0–30 Bar with 0.1% uncertainty) are connected to the bottom wall locating 50 and 60 mm upstream and downstream from the throat. As can be seen in the visible-light image (Fig. 2d), the cavitated multiphase flow was generated from the Venturi's throat, shown as the white cavity cloud which hides its internal information.

3. Results and discussion

3.1. Raw images of multiphase flow containing bubbles and particles

A typical X-ray image is converted to a digital photograph which is a numeric representation of a two-dimensional function, as shown in Fig. 3. Due to the absorption contrast and phase contrast mechanisms, the vapor bubbles and seeded particles can be distinguished from the liquid background. The absorption contrast results from the differences in the energy absorption/attenuation of X-ray after penetrating liquid, bubbles, or glass particles with different absorption coefficients. The X-ray converted image is represented by the intensity at a particular point whose pixel value is related to the remaining X-ray energy on the film after absorption. Due to this absorption contrast, the internal intensity or the pixel value of objects (bubbles and particles) is proportional to X-ray energy relieved, which is higher than the surrounding liquid.

The phase-contrast effect causes interference between contiguous points of the wavefront at a fixed distance from the investigated region of interest. As stated by Khaire and Shelkikar (2013), the difference in luminance that distinguishes an object is called contrast. The difference in hue and brightness between different objects within the same field of view determines the contrast in visual perception of the real world. When the diffracted X-ray from the liquid/vapor and liquid/glass interfaces reach the X-ray detector, they interfere with non-diffracted X-rays. The bubbles/glasses act as microscopic X-ray lenses, causing the incident plane wave to converge and be detected by the scintillator (Wildenschild and Sheppard, 2013). Because of the Fresnel diffraction, the sharp contrast at the periphery of a bubble is created as shown in the red circle in Fig. 3. In order for these interferences to occur, the beam must be spatially or at least partially coherent. Such a criterion can be readily met by a third-generation synchrotron system like the one at Argonne National Laboratory.
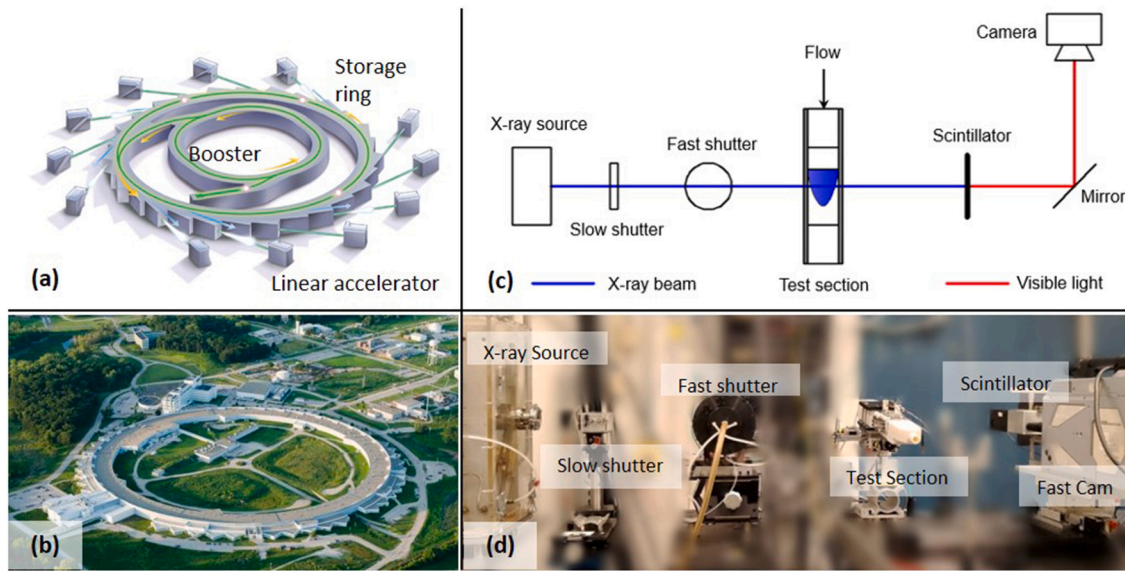
Fig. 1. (a) Sketch of the APS Synchrotron Radiation Facility. (b) Aerial photo of APS. (c) Diagram of path of light beams and X-ray imaging devices. (d) Image of the X-ray imaging devices with background blurred.
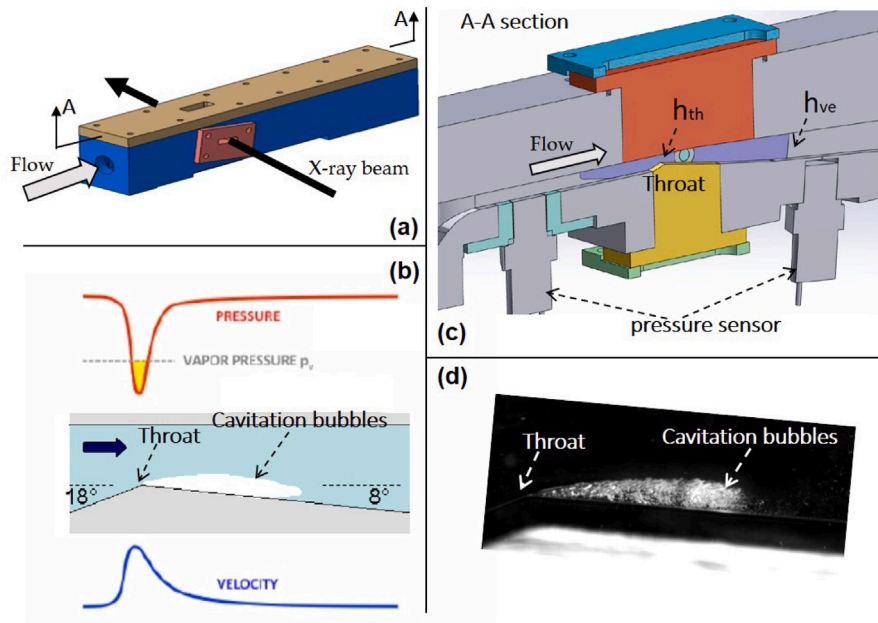

Fig. 2. (a) Profile of Venturi-type flow channel with flow direction and beam path shown. (b) Sketch of the convergent-divergent channel generating cavitation. (c) A-A cross-section of the convergent-divergent channel with dimensions labeled. (d) Visible-light image of cavitation bubbles.

3.2. Particle extraction based on raw X-ray images

As shown in Fig. 4, the complete image for a sheet cavity is reconstructed at different positions with spatially successive snapshots which are not acquired simultaneously. That is because the effective illuminating cross-section of the X-ray beam is limited to 1.7 mm × 1.3 mm, which is smaller than the cavity length around 20 mm. Image processing is necessary to detect the tracer particle from the vapor structures and liquid background. In order to proceed with the velocimetry methods and assess the dynamics of different phases independently, three new subplots must be made from each X-ray radiograph: (1) a vapor structure image without surfaces or particles for vapor volume fraction measurements; (2) a bubble image for vapor phase velocity measurements; and (3) a pure particle picture for liquid phase velocity measurements (Khlifa et al., 2017).

Multiple image processing algorithms have been developed for the identification of tracers in X-ray image (Zhang et al., 2020). Since a general or local threshold of the gray level was found inadequate to distinguish the objects, the edges generated from phase-contrast effects need to be detected (Zhang et al., 2019). Before performing experiments with bubbles, a pre-experimental test without cavitating flow input is performed to obtain a background image. The background image is then removed by images with bubbles to remove any unwanted background noise. To eliminate the holes inside and noise around bubble structures, the hole filling and median filtering methods are used. Finally, edge detection using the Canny method was conducted directly on the raw image to generate the outline of a bubble. Followed by morphological operation, noise delamination, and watershed of coalesced objects, 652 particles can be detected as in Fig. 5. It should be noted that the image I0 always corresponds
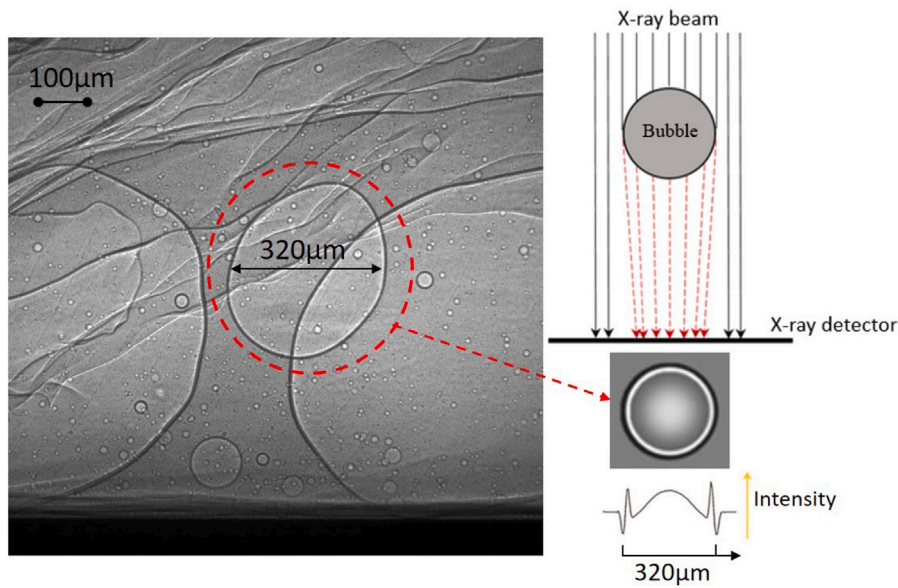
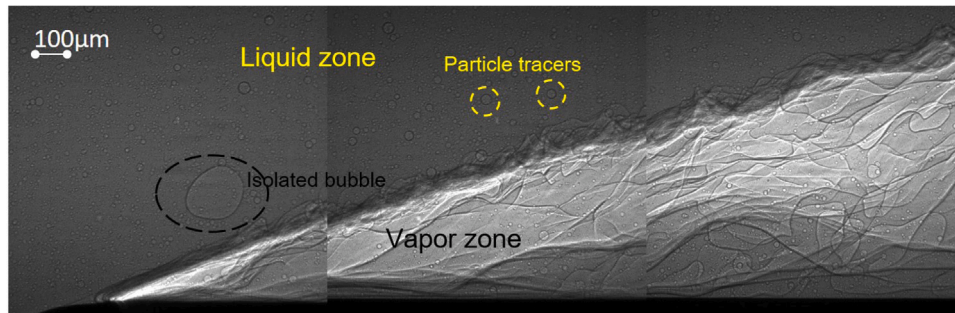**Fig. 3.** Detectable edges of bubbles based on the phase contrast mechanism of X-ray imaging.

Fig. 4. A cavity sheet reconstructed from the first 3 positions in the Venturi flow channel.
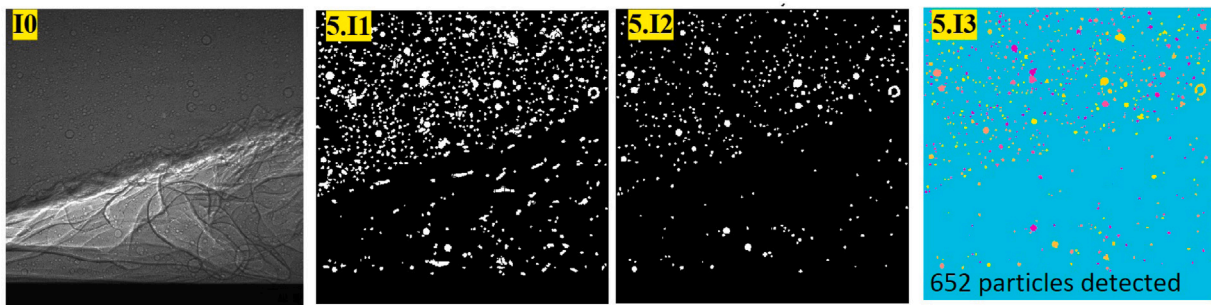

Fig. 5. Edge detection on X-ray image without contrast enhancement. I0: raw image; 5.I1: particles detected with edge watershed; 5.I2: particles filtered based on the eccentricity of 0.5; 5.I2: final 652 particles.

to the original image and will be labeled the same as I0 hereinafter. However, the particles inside the vapor zone are not detected properly. As reported in the literature (Zang et al., 2018), the accuracy of the method was calibrated by using a standardized solid sphere which showed the error for area calculation is smaller than 3.0%.

3.3. Particle extraction based on FT and WT enhanced images

The Fourier transform (FT) based Gaussian filtering and wavelet transform (WT) filtering can be applied to enhance raw X-ray images (Karathanassis et al., 2018). In the spectral domain as shown in Fig. 6, the raw image $I0$ is firstly noise filtered as image $6.I1$,

and then $6.I1$ is divided into low-pass filtered image $6.I2$ and high-pass filtered image $6.I3$. With Gaussian filtering, the high-pass image with interface information can be enhanced. Therefore, the intensity of the high-pass image $6.I3$ is multiplied by 2 and fused (i.e., added together) with the low-pass image $6.I2$ to obtain the contrast-enhanced image $6.I4$. The edge detection and morphology operation were applied on the contrast-enhanced image $6.I4$ and 682 particles are detected in particle image $6.I5$. After phase congruency, the cavity interphase seemed significantly brighter than the rest of the image. Therefore the image can be binarized by applying a mean filter and suitable thresholding.
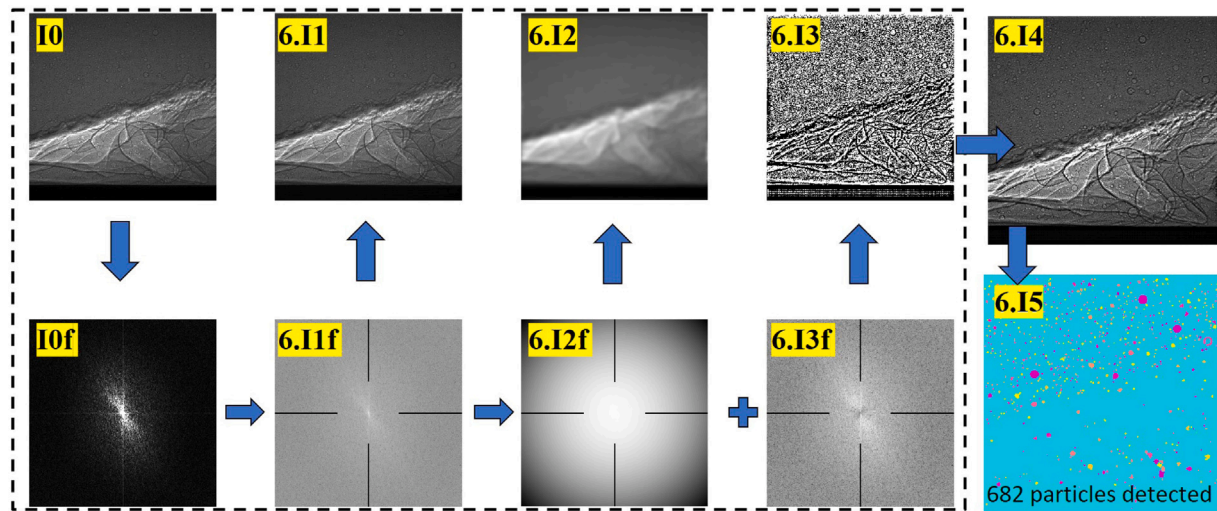
Fig. 6. Edge detection on X-ray image with Gaussian filtering contrast enhancement. I0: raw image; I1: noise filtered image; 6.I2: low-pass image; 6.I3: high-pass image; 6.I4: contrast-enhanced image; 6.I5: 682 particles detected; I0f: spectral plot of I0; 6.I1f: log plot of I0f; 6.I2f: low-frequency component; 6.I3f: high-frequency component.

Wavelet decomposition is a popular technique for denoising two-dimensional signals like pictures. Among various WT methods, the discrete wavelet transform (DWT) is based on the basis decomposition, while the stationary wavelet transform (SWT) is based on the frame decomposition, which means DWT is of minimum redundancy and SWT is much redundant. This study uses the stationary wavelet transform (SWT) to extract features since SWT can be used with images of any size, whereas DWT is best used with discrete signals from images size of a power of 2 (Zhang et al., 2010). At different levels or subbands, SWT can decompose the images into the approximation and the detail components. Fig. 7 shows the results of decomposing an input image into different subband images, under the wavelet transform with a db5 wavelet function and the 5-level SWT method. The detail component includes high-frequency signals like noise, which can be removed with suitable thresholds.

Compared with the large area of formed vapor phase and background of the liquid phase, the particle intensity varies quite quickly over space in this scenario. As a result, by executing the multi-level wavelet decomposition, removing particles can be thought of as a step of image de-noising. Since the edges of particles play a significant role in PIV, it is critical to separate these high-frequency edges' information from the low-frequency background and improve the quality of the time-resolved images. The highlighted image $a5$ is the approximation component, whereas the highlighted image $sum(d1 : d5)$ represents the detail component, which contains particle and vapor bubble edge information. By looking at the approximation component $a5$, it is seen that all particles have been filtered out and no relevant signals are left, thus no further decomposition is required. The high-frequency component of the images (e.g. edge of particles) is stored in the detail component as illustrated.

The Canny edge detector utilizing image intensity gradients is applied on detecting the detail components after WT decomposition. It can isolate sharp and clear edges that are smoothly linked to their neighborhoods. As shown in Fig. 8, the enclosed area by the identified edges is filled and given as a binary image, where the pixel with value 1 represents the position occupied by a particle in image $8.I1$. To assist the next morphological processes and generate the open-line suppressed image $8.I2$, the isolated short edge can be eliminated using the morphological opening process.

$8.I3$ illustrates the preliminary detection of particles based on the following criteria: (1) the eccentricities of objects cannot be over 0.5 since the particles are regular spheres; (2) the diameters of objects cannot be over 25 pixels, since the particles' sizes are normally less than 50 μm. As a result, filters based on the shape and sizes of the tracer particles can be utilized to eliminate the abnormal dots created by vapor bubbles or other noises. The removed abnormal objects and vapor structures are shown in the image $8.I4$. Because some particles may still be hidden in these deleted structures, a slightly stricter threshold was adopted in the secondary Canny edge detection step in $8.I4$ to identify the omissive particles as illustrated in $8.I5$. The ultimate detection of the particles on the detail component after wavelet decomposition is shown in the image $8.I6$, in which 628 dotted objects are extracted.

3.4. Images fused to execute velocimetry and densitometry

All tracer particles detected from Figs. 5, 6, and 8, (i.e. $5.I3$, $6.I5$, and $8.I6$) are fused to obtain the combined particle image $9.I4$ as shown in Fig. 9. This image fusion uses a linear combination of $5.I3$, $6.I5$, and $8.I6$ to produce enhanced images while keeping the image's details illuminated. The detected particle number is 1111 which is critical in calculating the interrogation window sizes in the PIV process. Here this amount of particles is sufficient (≥ 10 particles in a 50×50 pixels interrogation window) for the cross-correlation algorithm of the particle image velocimetry. In terms of the contrast and brightness of X-ray images, the suggested approach shows improved performance on a variety of datasets and has also been validated for standard laser PIV evaluation (Ge et al., 2022c,a).

$9.I4$ in Fig. 9 is a binarized image that displays a combination of particles (while coloring) identified from the dark background. To perform particle image velocimetry, all tracer particles need to be restored based on the detected location from the raw image $I0$. Finally, the image $9.I5$ depicts the processed results of the particle collection, which can be applied to flow velocity measurements. The identified particles in $9.I5$ were deleted from the raw X-ray picture $I0$ after equalizing the intensity by replacing the local average intensity with their neighborhood to create pure-vapor images. $9.I6$ is the processed image of vapor structures, that can be utilized to measure the vapor phase's instantaneous void fraction fields.

In order to achieve particle image velocimetry, the fluid is seeded with tracer particles that are assumed to faithfully follow the flow dynamics by evaluating the Stokes number (Gao et al., 2015). Under X-ray phase contrast mechanism, the fluid containing entrained particles is 'illuminated', making the particles visible. These particles are shown as white dots with high gray levels on the process image $9.I4$ as shown in Fig. 10(a). The motion of seeded particles can be used to calculate the flow's speed and direction in the velocity fields through applying the PIV algorithm (e.g., 'PIVlab' open-source toolbox) on processed particle images. Based on the location differences between
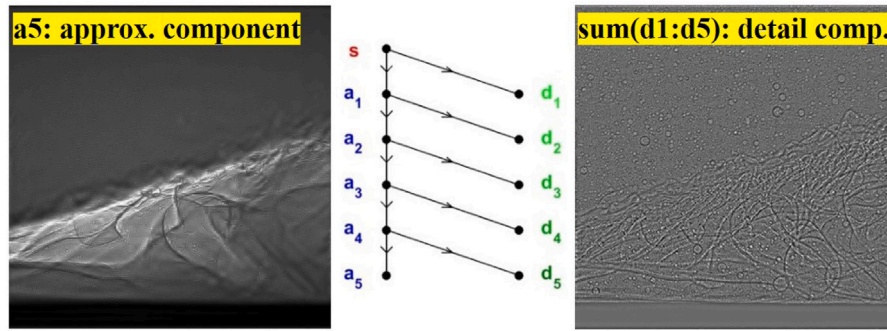
Fig. 7. Wavelet decomposition on X-ray images. a5: approximation component after 5-level db5 wavelet decomposition; sum(d1:d5): detail component after removing the approximation component from the raw image.
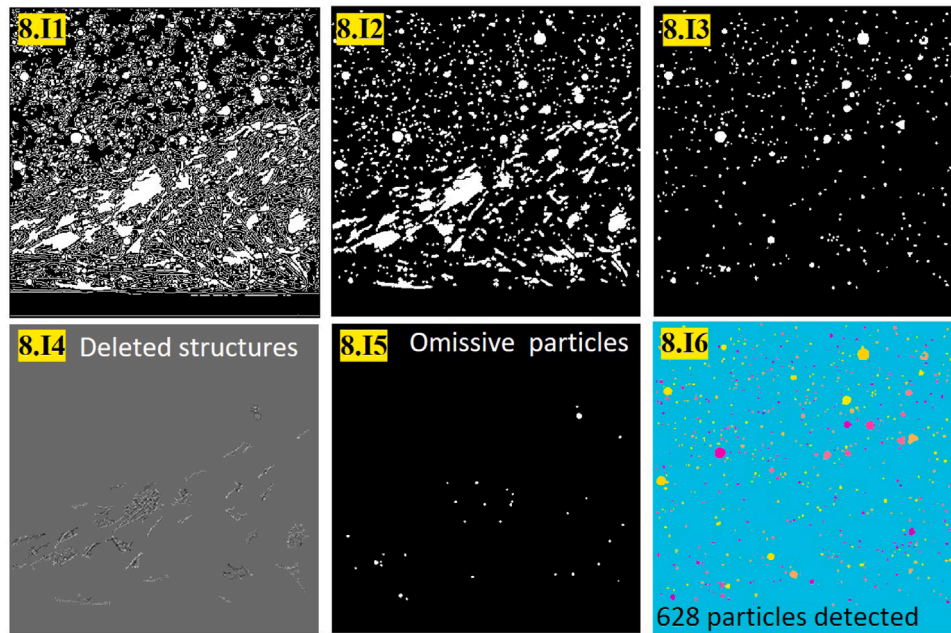

Fig. 8. Particle detection on the detail component after wavelet decomposition. 8.I1: edge detection by Canny edge detector; 8.I2: suppression of open lines; 8.I3: preliminary particle extraction using prescribed criteria; 8.I4: removed structures shown in gray level plot; 8.I5: omissive particles in the deleted structures; 8.I6: final 628 particles detected.

the pair of consecutive particle images (9.I5 at $t = 0$ and at t = 3.68 µs), the quantitative speed of flows can be measured by dividing the motion distance of particles by the time interval of 3.68 µs. The velocity uncertainty can be evaluated by applying the above-mentioned image processing and PIV algorithm on synthetic images similar to raw X-ray images (Khlifa et al., 2017). Results reveal that the averaged uncertainty of the flow velocity measurement is ±0.5 m/s, which is 3.3% considering a referenced freestream velocity of 15 m/s in this flow condition. Nevertheless, several limitations need to be highlighted that the X-ray PIV gives a projected velocity field containing accumulated flow information in the spanwise direction. Therefore, X-ray PIV results shall be compared with 2D laser PIV in order to illustrate the degree of flow three-dimensionality caused by the turbulent boundary layers on the two side walls in future works.

The volume fraction of the gas or void fraction is an important parameter in the design and operation of two-phase flow systems. Along the X-ray beam routes traversing the flow channel, the void fraction α of multiphase flow can be defined as the ratio of the vapor volumes to the total flow volumes. This α number represents the mean void fractions of the flow in the spanwise directions of the channel. After intensity equalization and neighborhood smoothing, the detected particles are eliminated from the initial image to obtain the liquid/vapor-only images. The processed image of vapor structures I_α

utilized to determine the instantaneous void fraction fields are shown in Fig. 10(b). The Eq. (1) is used to determine the vapor volume fraction α locally and quantitatively. It is derived from Lambert–Beer's law, based on the fact that the liquid and the vapor have different X-ray attenuation coefficients (Zhang et al., 2020).

$$\alpha = 1 - \frac{\ln\left(I_a/I_\alpha\right)}{\ln\left(I_a/I_b\right)} \tag{1}$$

Here, I_α represents the local gray-level intensity measured when the flow channel generating multiphase mixtures with bubbles and liquid; I_b represents the local intensity recorded when the test section is full of pure liquid; and I_a represents the local intensity measured when the test section is filled with the pure gas phase. As shown in Fig. 10 (right), the maximum void fraction is around 85% located at the interface between liquid and vapor zones, with the measurement uncertainty of about 2%.

4. Conclusion

In this paper, the ultra-fast X-ray imaging technique is used to analyze the turbulent cavitating flow in the Venturi's channel. The vapor structures and liquid tracer particles are both visible and detected after contrast enhancement of X-ray images. The particle image
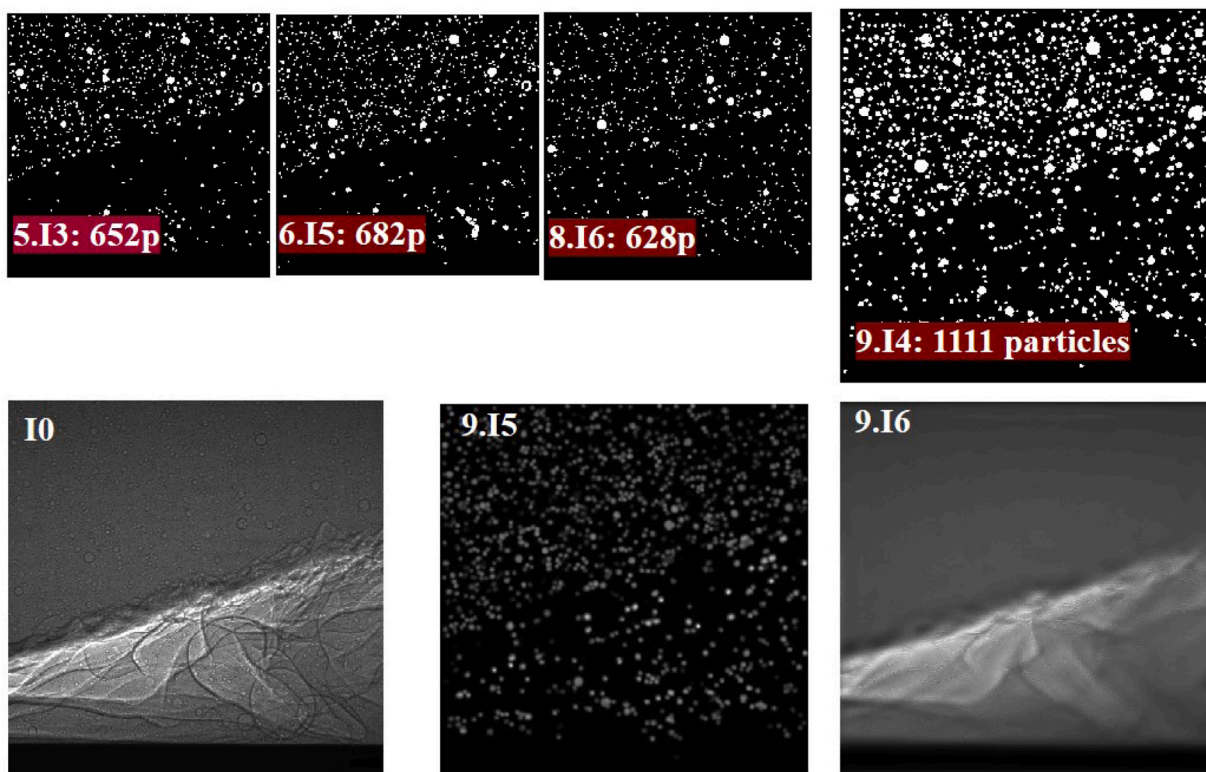
Fig. 9. Combined image 9.*I*4 of particles detected from contrast enhanced images (5.*I*3, 6.*I*5, and 8.*I*6) to obtain the velocimetry-used image 9.*I*5 and vapor-structure only image 9.*I*6.

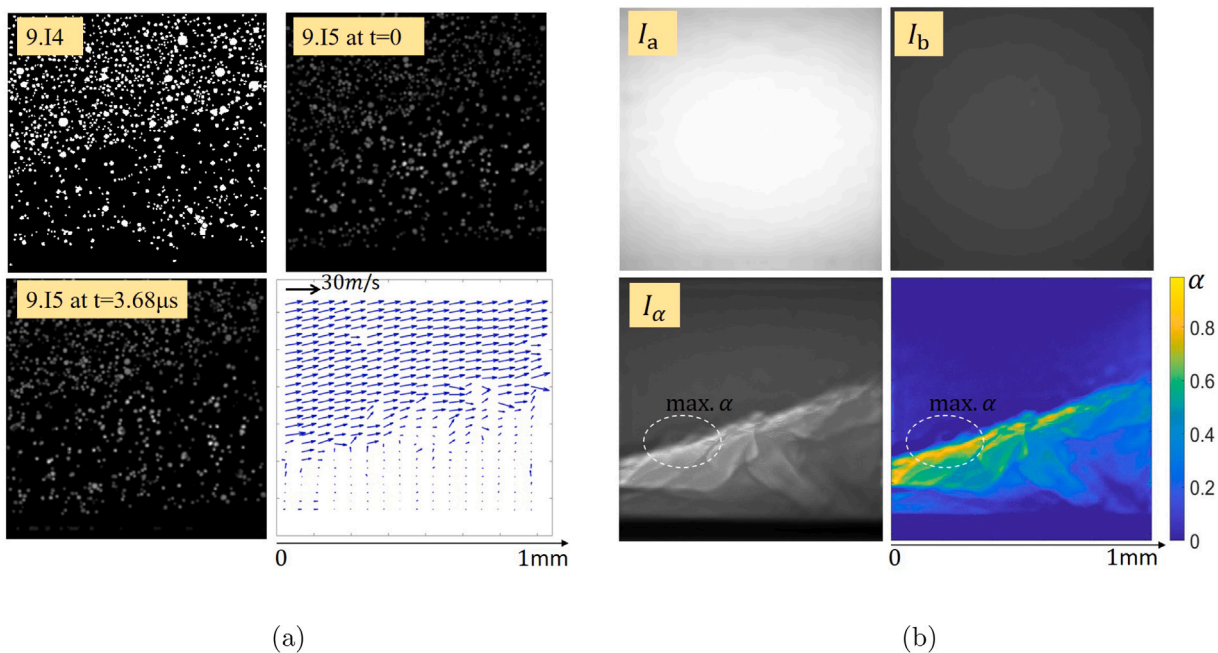(a)   (b)

Fig. 10. Sample results of (a) the flow velocity fields derived from particle image velocimetry, and (b) the void fraction fields of vapor phase.

velocimetry and densitometry based on void fraction estimation can thus be performed. Results show that the X-ray's attenuation effects can be used to measure the void fraction of multiphase flow and calculate velocity fields simultaneously. The developed image processing method using FT and WT decomposition algorithm is proved to be robust and valid for detecting the edges of particles and vapor structures in a cavitating flow. Based on the capture of instantaneous velocity and void fraction fields simultaneously, the analysis of fluid dynamics inside the opaque cavitation area and vapor structures outside the liquid flow will be accomplished in future works.

CRediT authorship contribution statement

Mingming Ge: Conceptualization, Data curation, Formal analysis, Writing – original draft. **Chuanyu Sun:** Investigation, Supervision, Methodology, Project administration. **Xinlei Zhang:** Software,

References

Aliseda, A., Heindel, T.J., 2021. X-Ray flow visualization in multiphase flows. Annu. Rev. Fluid Mech. 53, 543–567.

Cotte, M., Genty-Vincent, A., Janssens, K., Susini, J., 2018. Applications of synchrotron X-ray nano-probes in the field of cultural heritage. Comptes Rendus Physique 19 (7), 575–588.

Coutier-Delgosha, O., Devillers, J.-F., Pichon, T., Vabre, A., Woo, R., Legoupil, S., 2006. Internal structure and dynamics of sheet cavitation. Phys. Fluids 18 (1), 017103.

Coutier-Delgosha, O., Stutz, B., Vabre, A., Legoupil, S., 2007. Analysis of cavitating flow structure by experimental and numerical investigations. J. Fluid Mech. 578, 171–222.

Coutier-Delgosha, O., Vabre, A., Hocevar, M., Delion, R., Dazin, A., Lazaro, D., Gmar, M., Fezzaa, K., Lee, W., 2009. Local measurements in cavitating flow by ultra-fast X-ray imaging. In: Fluids Engineering Division Summer Meeting. Vol. 43734, pp. 371–379.

Fifield, L.S., Pharr, M., Staack, D., Pillai, S.D., Nichols, L., McCoy, J., Faucette, T., Bisel, T.T., Huang, M., Hasan, M.K., et al., 2021. Direct comparison of gamma, electron beam and X-ray irradiation doses on characteristics of low-density polyethylene, polypropylene homopolymer, polyolefin elastomer and chlorobutyl rubber medical device polymers. Radiat. Phys. Chem. 186, 109505.

Flannigan, D.J., Suslick, K.S., 2005. Plasma formation and temperature measurement during single-bubble cavitation. Nature 434 (7029), 52–55.

Ganesh, H., Mäkiharju, S.A., Ceccio, S.L., 2016. Bubbly shock propagation as a mechanism for sheet-to-cloud transition of partial cavities. J. Fluid Mech. 802, 37–78.

Gao, W., Mogi, T., Rong, J., Yu, J., Yan, X., Dobashi, R., 2015. Motion behaviors of the unburned particles ahead of flame front in hexadecanol dust explosion. Powder Technol. 271, 125–133.

Ge, M., Manikkam, P., Ghossein, J., Kumar, R., Coutier-Delgosha, O., Zhang, G., 2022a. Dynamic mode decomposition to classify cavitating flow regimes induced by thermodynamic effects. Energy 124426.

Ge, M., Petkovšek, M., Zhang, G., Jacobs, D., Coutier-Delgosha, O., 2021. Cavitation dynamics and thermodynamic effects at elevated temperatures in a small Venturi channel. Int. J. Heat Mass Transfer 170, 120970.

Ge, M., Sun, C., Zhang, G., Coutier-Delgosha, O., Fan, D., 2022b. Combined suppression effects on hydrodynamic cavitation performance in venturi-type reactor for process intensification. Ultrasonics Sonochemistry 106035.

Ge, M., Zhang, G., Petkovšek, M., Long, K., Coutier-Delgosha, O., 2022c. Intensity and regimes changing of hydrodynamic cavitation considering temperature effects. J. Cleaner Prod. 130470.

Karathanassis, I.K., Koukouvinis, P., Kontolatis, E., Lee, Z., Wang, J., Mitroglou, N., Gavaises, M., 2018. High-speed visualization of vortical cavitation using synchrotron radiation. J. Fluid Mech. 838, 148–164.

Khaire, M.G., Shelkikar, R., 2013. Resolution enhancement of images with interpolation and DWT–SWT wavelet domain components. Int. J. Appl. Innov. Eng. Manage. 2 (9), 242–248.

Khlifa, I., Vabre, A., Hočevar, M., Fezzaa, K., Fuzier, S., Roussette, O., Coutier-Delgosha, O., 2017. Fast X-ray imaging of cavitating flows. Exp. Fluids 58 (11), 1–22.

Ruiz-Vargas, A., Ivorra, A., Arkwright, J.W., 2018. Design, construction and validation of an electrical impedance probe with contact force and temperature sensors suitable for in-vivo measurements. Sci. Rep. 8 (1), 1–11.

Sætre, C., Tjugum, S.-A., Johansen, G.A., 2014. Tomographic segmentation in multiphase flow measurement. Radiat. Phys. Chem. 95, 420–423.

Salehi, F., Ghiji, M., Chen, L., 2020. Large eddy simulation of high pressure spray with the focus on injection pressure. Int. J. Heat Fluid Flow 82, 108551.

Salgado, C.M., Dam, R.S., Salgado, W.L., Santos, M.C., Schirru, R., 2021a. Development of a deep rectifier neural network for fluid volume fraction prediction in multiphase flows by gamma-ray densitometry. Radiat. Phys. Chem. 189, 109708.

Salgado, W., Dam, R., Salgado, C., Silva, A., 2022. Identification of the interface region in transport of petroleum by-products in polyducts using artificial neural network and gamma densitometry by the MCNPX code. Radiat. Phys. Chem. 192, 109908. http://dx.doi.org/10.1016/j.radphyschem.2021.109908, URL https://www.sciencedirect.com/science/article/pii/S0969806X21005582.

Salgado, C.M., de Freitas Dam, R.S., de Carvalho Conti, C., Salgado, W.L., 2021b. Three-phase flow meters based on X-rays and artificial neural network to measure the flow compositions. Flow Meas. Instrum. 82, 102075.

Sattari, M.A., Roshani, G.H., Hanus, R., 2020. Improving the structure of two-phase flow meter using feature extraction and GMDH neural network. Radiat. Phys. Chem. 171, 108725.

Wei, M., Gao, Y., Yan, F., Chen, L., Feng, L., Li, G., Zhang, C., 2017. Experimental study of cavitation formation and primary breakup for a biodiesel surrogate fuel (methyl butanoate) using transparent nozzle. Fuel 203, 690–699.

Wildenschild, D., Sheppard, A.P., 2013. X-ray imaging and analysis techniques for quantifying pore-scale structure and processes in subsurface porous medium systems. Adv. Water Resour. 51, 217–246.

Wu, X., Maheux, E., Chahine, G.L., 2017. An experimental study of sheet to cloud cavitation. Exp. Therm Fluid Sci. 83, 129–140.

Zambianchi, P., Hermógenes, G., Zambianchi, J., 2022. Quantification of gold nanoparticles using total reflection X-ray fluorescence by Monte Carlo simulation (MCNP code) applied to cancer cell research. Radiat. Phys. Chem. 193, 109937.

Zang, D., Li, L., Di, W., Zhang, Z., Ding, C., Chen, Z., Shen, W., Binks, B.P., Geng, X., 2018. Inducing drop to bubble transformation via resonance in ultrasound. Nature Commun. 9 (1), 1–7.

Zhang, X.-L., Ge, M.-M., Zhang, G.-J., Coutier-Delgosha, O., 2021. Compressible effects modeling for turbulent cavitating flow in a small venturi channel: An empirical turbulent eddy viscosity correction. Phys. Fluids 33 (3), 035148.

Zhang, G., Khlifa, I., Fezzaa, K., Ge, M., Coutier-Delgosha, O., 2020. Experimental investigation of internal two-phase flow structures and dynamics of quasi-stable sheet cavitation by fast synchrotron x-ray imaging. Phys. Fluids 32 (11), 113310.

Zhang, T., Qian, Y., Yin, J., Zhang, B., Wang, D., 2019. Experimental study on 3D bubble shape evolution in swirl flow. Exp. Therm Fluid Sci. 102, 368–375.

Zhang, Y., Wang, S., Huo, Y., Wu, L., Liu, A., 2010. Feature extraction of brain MRI by stationary wavelet transform and its applications. J. Biol. Systems 18 (spec01), 115–132.